Daxin Li
Dechang Jia
Zhihua Yang
Yu Zhou

SiBCN Ceramics and Composites Prepared by Mechanical Alloying

Springer

SiBCN Ceramics and Composites Prepared by Mechanical Alloying

Daxin Li · Dechang Jia · Zhihua Yang · Yu Zhou

SiBCN Ceramics and Composites Prepared by Mechanical Alloying

Springer

Daxin Li
School of Material Science and Engineering
Harbin Institute of Technology
Harbin, Heilongjiang, China

Dechang Jia
School of Material Science and Engineering
Harbin Institute of Technology
Harbin, Heilongjiang, China

Zhihua Yang
School of Material Science and Engineering
Harbin Institute of Technology
Harbin, Heilongjiang, China

Yu Zhou
School of Material Science and Engineering
Harbin Institute of Technology
Harbin, Heilongjiang, China

ISBN 978-981-97-3028-5 ISBN 978-981-97-3029-2 (eBook)
https://doi.org/10.1007/978-981-97-3029-2

Preface

The development of novel multifunctional thermal protection materials operated under harsh environments, typical of high-temperature oxidation, severe thermal shock, ablation by combustion gas flow, etc., is one of the urgent needs in modern aerospace industry. The amorphous Si-based multicomponent ceramics, such as SiCN, SiBN, SiBC, SiBCN, SiBON, SiBOCN, etc. have received much attention in recent years owing to their highly stable amorphous structures and specific properties different from the crystalline counterparts. Coincidently, the quaternary SiBCN system stands out from all recent materials offering great potentials at high temperatures due to their higher microstructural stability and excellent high-temperature properties including resistance to oxidation, thermal shock, creep and ablation.

In past 30 years, significant progress on the synthesis and fabrication of SiBCN ceramics through the precursor-derived ceramics (PDCs) route as an appropriate synthesis method for synthesizing multi-component materials have been made. The PDCs approach based on well-defined precursors can offer precise control over chemical composition, microstructure and ceramic shapes that have provided access to a vast number of SiBCN ceramics with interesting properties. In this aspect, the PDCs route is mostly technologically suitable for preparing ceramic films, coatings, fibers, porous structure or ceramic matrix composition (CMCs), with extremely homogeneous distribution of the constituting elements without near-range order.

By using inorganic powders (such as Si, graphite, boron, h-BN, etc.) instead of the organic precursor as raw materials, the inorganic processing route based on mechanical alloying (MA), one of the nonequilibrium processing techniques, coupled with sequential sintering, although apparently very "hard" compared to the "soft" PDCs method, is actually a simple and effective way to prepare monoliths with uniform microstructure and superior properties. It has been used to obtain dense SiBCN monoliths and structural parts stable at high-temperatures providing new experimental data and therefrom a more detailed understanding of the intrinsic properties of metastable SiBCN materials, benefitting progress toward engineering applications.

Herein this book mainly provides a comprehensive treatment of the MA-derived SiBCN (MA-SiBCN) ceramics and their CMCs, aspect of theme content including material design and preparation, microstructural feature and evolutionary process,

mechanical and thermophysical properties, resistance to oxidation, thermal shock and ablation, and the mechanisms of oxidation, ablation and crystallization of SiBCN-based materials. Chapter 1 introduces the motivation, structure characteristics, performance advantages and prospects of the SiBCN materials derived from PDCs or MA routes. Chapter 2 describes the basis of mechanical alloying, and outlines the historical prospective and principle of the non-equilibrium phases formation, and the alloying mechanism and amorphization kinetics of SiBCN. Chapter 3 includes the crystallization behavior and thermal stability of MA-derived amorphous SiBCN powders and also focuses on the effects of metals and/or ceramics particles on the microstructural evolution of the mixing inorganic powders. Chapter 4 introduces the densification kinetics and crystallization mechanisms of MA-SiBCN materials. This section also involves the comparison of sintering methods on densification and microstructural/morphological evolution of PDCs or MA-derived SiBCN. Chapter 5 deals with mechanical behavior and strengthening/toughening mechanisms in MA-SiBCN materials, focusing on the intrinsic toughness and brittle fracture of nanocrystalline or amorphous monoliths, and "additive" strengthened/toughened MA-SiBCN composite ceramics and CMCs. Chapter 6 outlines the thermal damage behavior and damage mechanisms of MA-SiBCN materials.

We wish to acknowledge all the contributing authors for their great enthusiasm in reviewing portions of the draft manuscript and providing photographs in their respective area of expertise. We also thank the financial supports from the National Key Research and Development Program (No. 2017YBB0310400), the National Natural Science Foundation-Innovation Research Group Project (No. 51621091), Outstanding Youth Funding (No. 51225203), Key Project Funding (Nos. 51832002, 52232004), General Funding (Nos. 52172068, 52372059, 51272300, 51072041), Youth Funding (Nos. 52002092, 50902031), and Heilong Jiang Natural Science Fund for Young Scholars (No. YQ2021E017). The financial supports by the Postdoctoral Innovation Talent Support Program (No. BX20190095), Heilongjiang Touyan Team Funding and Advanced Talents Scientific Research Foundation of Shenzhen: Yu Zhou, are also acknowledged.

At Science Park of Harbin
Institute of Technology
August 2024

Daxin Li
Dechang Jia

Contents

Chapter 1
Introduction

1.1 The Processing Route: Motivation, Principle and History

The aerospace industry is continually searching for lighter high-strength materials that perform under more and more extreme conditions. In particular there is considerable demand for structural materials and components that are stable to combustion gas flows, as leading edges and ablation shields. Such extreme conditions encountered in these applications mandate materials that integrate multiple properties including excellent mechanical properties (especially high tolerance to thermal and mechanical stress), high thermal stability, and superior resistance to thermal shock, oxidation and ablation to ensure their safety and reliability in service [1–6].

Currently, binary ceramics such as SiC and Si_3N_4 are used widely for high temperature applications due to their low density, high hardness, excellent mechanical properties and high thermo-chemical stability. However, the mechanical properties and oxidation resistance of SiC ceramics generally degrade in air above 1500 °C due to softening of protective SiO_2 oxide scale. Commercial Si_3N_4 components offer upper use temperatures of no more than 1300 °C in oxidizing environments [7–10]. Additionally, the high-temperature structural applications of the single-phase ultra-high temperature ceramics (UHTCs) such as ZrB_2 and HfB_2 are limited by their high density as well as poor damage tolerance detrimental to thermal shock resistance, although their unique combined properties, such as high melting points, high chemical inertness against molten metals, and good resistance to ablation, allow them to be potential candidates for nose cone and wing leading edges as thermal protection for reentry systems [11–15].

Consequently, there is a continuing search for superior materials building on what is currently state-of-the-art. These include carbide and nitride ceramic matrix composites (CMCs), multicomponent ceramics and their CMCs, such as C_f/(C, SiC, Si_3N_4) [16–20], SiC_f/(SiC, ZrB_2) [21–24], SiC_p/(Si_3N_4, ZrB_2, HfB_2) [25–28],

D. Li et al., *SiBCN Ceramics and Composites Prepared by Mechanical Alloying*,
https://doi.org/10.1007/978-981-97-3029-2_1

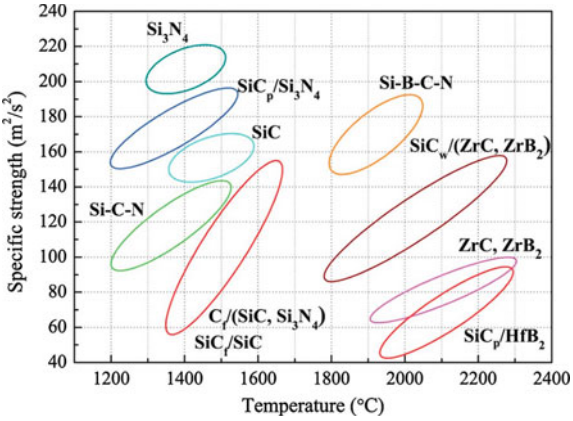

Fig. 1.1 Relationship between using temperature and specific strength of the commonly used structural ceramic materials [4]

SiC_w/(ZrC, ZrB_2) [29–31], SiCN [32–34], (C_f, SiC_f)/SiCN [35–37], SiBCN(-Zr, Hf, Al) [38–44], (C_f, SiC_f)/SiBCN [45–48], etc. Among them, metastable silicoboron carbonitride (SiBCN) ceramics have attracted considerable attention due to their exceptional microstructural stability, relatively higher specific strength and use temperature (Fig. 1.1) and satisfying high-temperature property retention.

Precursor-derived SiBCN fibers, one of the very first described SiBCN materials, remain amorphous at least up to 1800 °C, and do not undergo microstructural changes at this temperature. At temperatures up to 1600 °C, SiBCN ceramics show oxidation resistance superior to those of SiC and Si_3N_4. On exposure to air at 1500 °C for 50 h, the tensile strength of oxidized SiBCN fibers still reaches 2.5 GPa, as high as that (3.0 GPa) of the as-prepared fibers within the experimental error. In contrast, the residual tensile strength of oxidized SiC fibers with an overcoat of cristobalite approaches zero. Additionally, the resulting SiBCN ceramic fibers offer high elastic modulus at 1400 °C/Ar, a low coefficient of thermal expansion, good flexibility and low density [49, 50]. Interestingly, SiBCN fibers are the only fibers that seem to fulfill the rather ambitious requirements the potential users (European turbine producers) stated for so-called third generation fibers.

The development of quaternary SiBCN ceramics can be traced back to the precursor-derived SiC and Si_3N_4 [51, 52]. In the early '60s, Ainger [53] and Chantrell [54] have reported the synthesis of non-oxide ceramics derived from molecular precursors. In the early '70s, Verbeek [55, 56], Winter [57] and Yajima [58–61] developed sequentially the practical production of Si_3N_4/SiC and SiC ceramic fibers by transformation of polyorganosilicon compounds. Since then, the preparation of precursor-derived non-oxide ceramics has gained significant interest. Many efforts have been made to produce the classical binary ceramics (SiC and Si_3N_4) and multi-component materials (SiCN, SiBN, SiBCN). In 1985, Takamizawa [62–64] first synthesized the SiBCN precursors. Until the '90s, new breakthroughs were made in the development of precursor-derived ceramic monoliths with tailored microstructures and excellent properties. In the late '90s, Riedel et al. [42] reported processing of

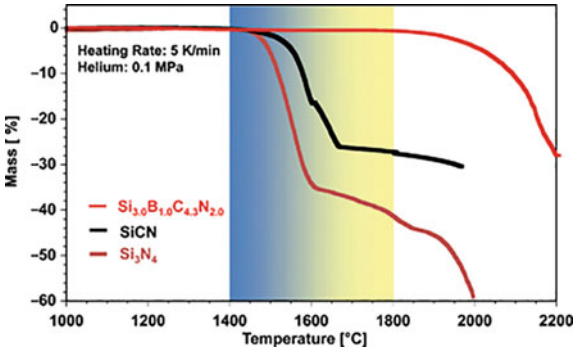

Fig. 1.2 The thermogravimetric curves of the precursor-derived SBCN, SiCN and Si_3N_4 ceramics when heated to 2000–2200 °C in an inert atmosphere [42]

SiBCN monoliths by precursor pyrolysis together with Si_3N_4, Si_3N_4/SiC and SiCN monoliths [65–67] (Fig. 1.2).

The development of SiBCN and SiBCN-Me (Me=Al, Ti, Zr, Hf, etc.) materials including precursor synthesis and ceramic processing has received much attention from researcher working on the chemistry and material science [68–71]. The preparation process can be generally divided into five steps: (1) Synthesis of the precursor by standard Schlenk techniques [72, 73]; (2) Crosslinking or curing; (3) Warm pressing (200–400 °C) of ground SiBCN precursor powders; (4) Thermolysis (1000–1400 °C) of warm pressed precursor shapes to obtain amorphous SiBCN ceramic shapes; (5) Post-annealing (temperatures up to 2000 °C) of amorphous ceramics to obtain polycrystalline nanocomposites [43, 74].

The chemical composition, microstructures and properties of precursor-derived ceramics SiBCN (PDCs-SiBCN) can be tailored effectively by controlling the initial reagent structures, chemical reactions and processing parameters. The thermolysis process generally proceeds at relatively low temperatures (1000–1400 °C) and the resulting polycrystalline SiBCN provides clean grain boundaries. The precursor-derived ceramic route (hereinafter referred to as the organic method) is the only mechanism for producing SiBCN fibers, films, monoliths and their ceramic matrix composites with addition of continuous fibers [75–82]. The investigation of PDCs-SiBCN materials over the last three decades continues to confirm their excellent properties, as noted above.

Unfortunately, the organic method also has some shortcomings that limit its widely commercial utility. The raw materials are usually expensive thus leading to high-cost products. Some organic solvents are harmful to human health and the environment. They are also flammable and present waste disposal problems. This processing route is also low-yield and complex. The microstructures and properties of final products are greatly influenced by multiple factors. The gas release and mass loss during pyrolysis requires careful monitoring to avoid porous structures and to carefully control shrinkage (even microcracks). These issues can be countermanded by addition of passive or active fillers (like ceramic or metal powders) to minimize shrinkage during pyrolysis [41, 83–85]. The organic method can be problematic when used to fabricate dense SiBCN monoliths and structural parts, although the vacuum-assisted

polymer infiltration [45, 46], pressure-assisted pyrolysis [86], and sintering [87–89] have recently received attention and can offer better processing than simple precursor processing. Thus, there is considerable motivation to develop new and complementary processing routes.

As a relatively low-cost and simple approach to monoliths, Jia et al. [90] proposed in 2004 using mechanical alloying (MA) as a novel inorganic processing route to fabricate dense SiBCN ceramics. Amorphous SiBCN powders are synthesized by simple, high energy mechanical alloying using inorganic elemental powders (cubic silicon, hexagonal boron nitride, graphite, boron, aluminum, zirconium, hafnium, etc.) as starting materials, and then sintered by hot pressing (HP), or spark plasma sintering (SPS) or hot-isostatic pressing (HIP) to produce fully dense monoliths. The only drawback to this approach is the need for high sintering temperatures up to 1700–2000 °C and crystallization of the intermediate amorphous powders which cannot be avoided. So, nanocrystalline microstructures with residual amorphous phases are obtained eventually similar to those of nanocrystalline SiBCN materials developed by precursor pyrolysis after higher temperature treatment.

Note that recent use of high-pressure synthesis technique provides quite dense and completely amorphous SiBCN monoliths the first to be prepared at high pressures and low temperatures. The inorganic processing route has proven simple and effective for preparing SiBCN monoliths and structural parts with the uniform microstructures and good properties. This processing route readily provides centimeter-sized samples convenient for evaluating basic properties and thus complements the precursor route especially for producing SiBCN monoliths. Alternatives to the precursor and inorganic methods include chemical vapor deposition (CVD) [91–94], reactive magnetron sputtering [75–77] and sol–gel processing [95]. The development of PDCs-SiBCN ceramics processing has been reviewed by Jansen [50] and Baldus [49, 96], Kroke and Li [97], Bill [98], Riedel [74] and Colombo [42], and Viard [99]. Coincidently, the phase equilibria and material thermodynamics of PDCs-SiBCN coupled with the ternary systems (SiBN, SiBC, SiCN) were summarized by Aldinger and Seifert [100].

1.2 Crystallization and Phase Equilibrium in Amorphous SiBCN

The outstanding structural stability at high-temperatures, and good resistance to oxidation (Fig. 1.3) and creep are the main features of the amorphous PDCs-SBCN materials. Apparently, the temperature stability of the PDCs-SBCN is limited and strongly depends on the particular ceramic composition and presence of strong 3-D amorphous covalent network structures [101–103].

Generally, these amorphous PDCs-SiBCN materials contain amorphous Si–C-N domains related with regions of amorphous domains composed of stacked layers containing carbon, boron, and nitrogen (turbostratic B-N-C domains) [104]. Further

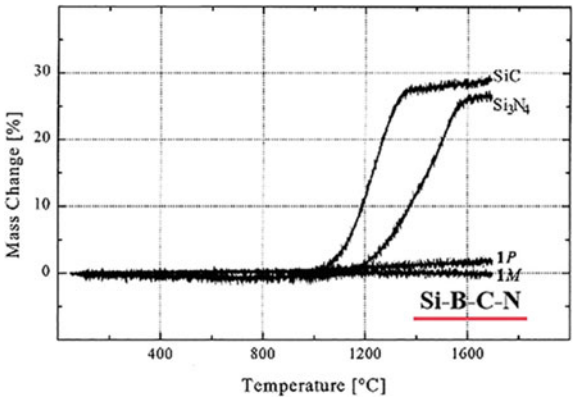

Fig. 1.3 The thermogravimetric curves of the amorphous PDCs-SiBCN, crystalline SiC and crystalline Si_3N_4 ceramics when heated to 1650 °C in flowing air [81]

annealing of the as-thermolyzed PDCs-SiBCN at temperatures $T \geq 1400$ °C leads to the formation of SiC nanocrystallites [105, 106], as the primary crystalline phase, within the amorphous microstructure. Si_3N_4 nanocrystallites emerge at significantly higher temperatures, depending on the boron content. In this connection, the increase in boron content up to 8–9 at% retards the crystallization of Si_3N_4 [107], whereas the crystallization of SiC is promoted with addition of the boron content (Fig. 1.4). The available thermodynamic model of amorphous Si-C-N domains, nanocrystalline Si_3N_4, and nanocrystalline SiC treated as the separated phases with variable dimensions were proposed by Tavakoli [108] to the as-forementioned kinetic crystallization process. Note that this thermodynamic model approach comprises of both nucleation and growth processes, which are connected with kinetic aspects of crystallization.

Clear information on phase equilibria in PDCs-SiBCN system at constant temperatures can be derived from calculated quaternary isothermal sections. Concentration sections through the 1673 and 2273 K tetrahedra at 10 at% boron were calculated by Seifert et al. [100] (Fig. 1.5). In both cases the (regular) concentration tetrahedron is divided into different distorted tetrahedra indicating the four-phase equilibria at the specific temperature. The phase equilibria and composition of some high temperature ($T > 2273$ K) stable PDCs-SiBCN PMBS(m), PHBS(p), PHBS(m), PMBS(p)

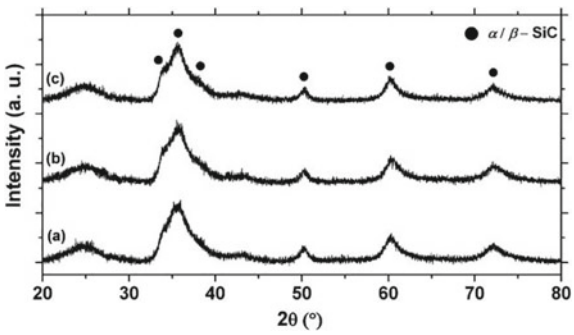

Fig. 1.4 XRD patterns of the PDCs-SiBCN system: **a** 3.7 at% B; **b** 6.0 at% B; **c** 8.3 at% B prior to the crystallization of Si_3N_4 after isothermal heat treatment at $T = 1700$ °C for 2, 6, and 15 h, respectively [107]

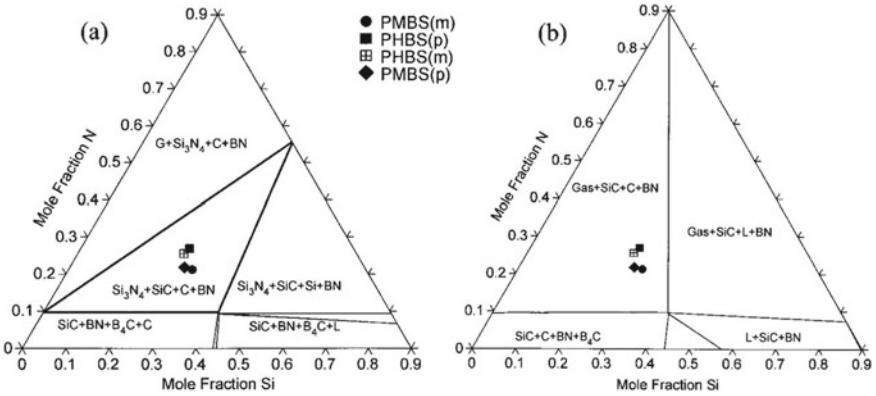

Fig. 1.5 Concentration sections in the PDCs-SiBCN system at constant boron content (~ 10 at%) and temperature: **a** $T = 1673$ K; **b** $T = 2273$ K [100]

are indicated (all with ~ 10 at% boron content). At $T = 1673$ K, they are all located in the phase field $Si_3N_4 + SiC + C + BN$. This phase equilibrium remains stable as low as room temperature. However, at high temperatures (e.g., 2273 K) the composition is located in the phase field Gas + SiC + C + BN, and some decomposition is expected.

The phase fraction diagrams computed by Thermo-Calc software [109] for the composition of the PDCs-SiCN and PDCs-SiBCN have been compared (Fig. 1.6) [101]. In these calculations, the hydrogen content of the ceramics was ignored, assuming hydrogen exists in the form of H_2 gas at temperatures $T > 1050$ °C [99]. The equilibrium state of the PDCs-$SiC_{1.4}N_{0.9}$ consists of three phases SiC, Si_3N_4 and C at low temperatures ($T < 1484$ °C), and its thermal stability is limited by the carbothermal reduction of Si_3N_4 with C at $T = 1484$ °C. As expressed, this reaction results in the formation of SiC and a mass loss of the solid phase due to the gas (N_2) escape. Consequently, the new phase equilibrium is obtained at $T >$ 1484 °C, including SiC, C and N_2. This equilibrium state remains unchanged up to the maximum temperature of calculation $T = 2000$ °C.

The main difference between the phase fraction diagrams computed for the PDCs-$SiC_{1.4}N_{0.9}$ and PDCs-$SiC_{1.5}N_{1.0}B_{0.05}$ materials is the emergence of the additional phase BN and the consequential formation of the four-phase equilibrium SiC + Si_3N_4 + C + BN for the boron-containing ceramics [101]. However, the same reaction as explained above for PDCs-$SiC_{1.4}N_{0.9}$ also determines the stability of PDCs-$SiC_{1.5}N_{1.0}B_{0.05}$. Since BN is very stable within the computed temperature range, the amount of BN phase remains unchanged and consequently, the three-phase equilibrium including SiC, C and BN is anticipated at the temperature range between 1484 and 2000 °C for the PDCs-$SiC_{1.5}N_{1.0}B_{0.05}$. Note that BN phase regarded as non-interacting with other phases in this PDCs-SiBCN system to generate the computed phase fraction diagrams may be considered insufficiently, since the amorphous

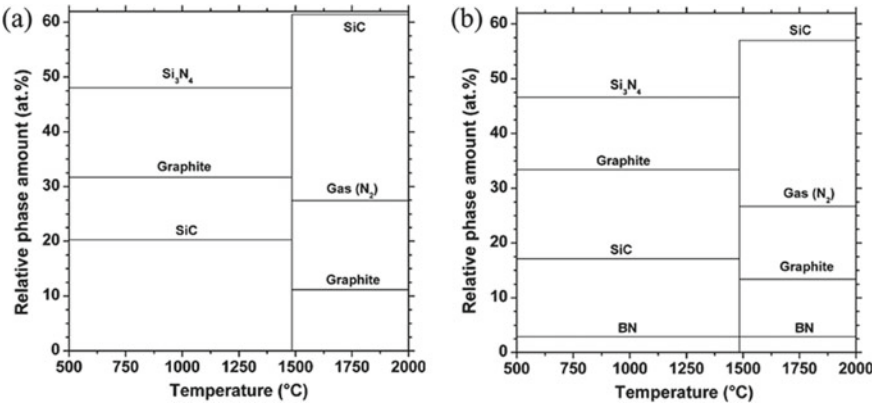

Fig. 1.6 The computed phase fraction diagrams: **a** PDCs-$SiC_{1.4}N_{0.9}$; **b** PDCs-$SiC_{1.5}N_{1.0}B_{0.05}$ (hydrogen content in ceramics was ignored) [101]

domains of Si-C-N and B-C-N must interact on each other during crystallization process.

1.3 Microstructure and Performance Characteristics of SiBCN

1.3.1 Overview of Microstructural Features

The microstructural features of the mechanical alloying SiBCN (MA-SiBCN) nanocrystalline ceramics are extremely similar to those of the precursor-derived counterparts. The chemical composition of the studied MA-Si_2BC_3N is approximately located on the triple-phase line of SiC, BN and C. Consequently, crystalline MA-Si_2BC_3N ceramics should consist mainly of SiC and BN(C), confirmed experimentally. The PDCs-SiBCN nanocrystalline ceramics consist of the same phases especially when the chemical composition is located in the four-phase field of SiC + BN + C + B_4C. Coincidently, the encapsulation of SiC by BN(C), the turbostratic structure of BN(C) and "clean" grain boundaries are common features to the two "types" of crystalline SiBCN materials.

The only difference is that other phases including Si_3N_4, SiC_xN_y, B_4C, Si likely form in PDCs-SiBCN system depending on initial chemical composition and processing. For example [110], a PDCs-SiBCN ceramic particle with a chemical composition of $Si_{24}B_8C_{44}N_{24}$ obtained by hydroboration of oligovinylsilazane is composed of Si_3N_4 and SiC nanocrystallites which are embedded in a turbostratic BNC_x matrix after being annealed at 1800 °C for 10 h in N_2 (Fig. 1.7). However, another PDCs-SiBCN ceramic monoliths pyrolyzed at 1400 °C for 2 h in Ar derived

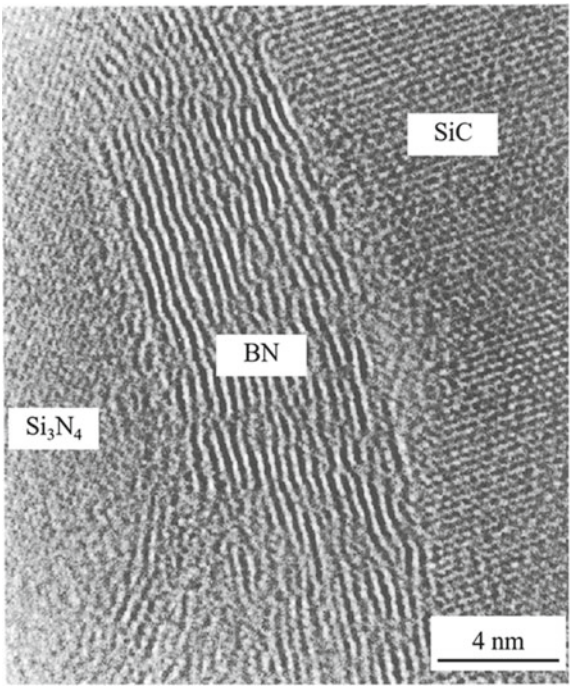

Fig. 1.7 The typical microstructure composed of the nano SiC, Si_3N_4 and turbostratic BN(C) for a crystallized PDCs-SBCN material [110]

from a boron-modified polyvinylsilazane remain amorphous but form α-SiC crystals of a mean grain size of ~ 100 nm embedded in a turbostratic BNC_x matrix after annealing at 1800 °C for 3 h in N_2.

Note that, nitrogen cannot be added independently in MA so that the composition design is less flexible [111]. Additionally, it is likely difficult to produce powders by MA with extremely uniform elemental distribution and strong chemical bonds, like that in PDCs route [112]. As a result, MA derived amorphous SiBCN powders exhibit a relatively low initial temperature of crystallization. However, the dense MA-SiBCN monolithic ceramics with a relatively large dimension can be easily prepared by this inorganic route thus facilitating the material property evaluation.

Both β-SiC and α-SiC form in hot-pressed MA-Si_2BC_3N at 1900 °C. The SiC grains are nearly equiaxed with average grain size (AGS) of ca.100 nm [113–115]. Most β-SiC grains are well developed with a high degree of crystallinity. A few β-SiC grains contain stacking faults, which is common in β-SiC single crystals, whiskers, nanowires and monoliths. These defects are usually found in the (111) plane acting as the primary fault plane. The α-SiC content is relatively low compared with β-SiC. They have similar shape, size and stacking faults. However, α-SiC grains show hexagonal wurtzite structure and their (0002) planes contain most of the stacking faults (Fig. 1.8).

BN(C) grains have no fixed shape and are uniformly distributed around SiC grains [114]. Most are 15–50 nm thick. A few larger ones with AGS of ca. 100 nm also

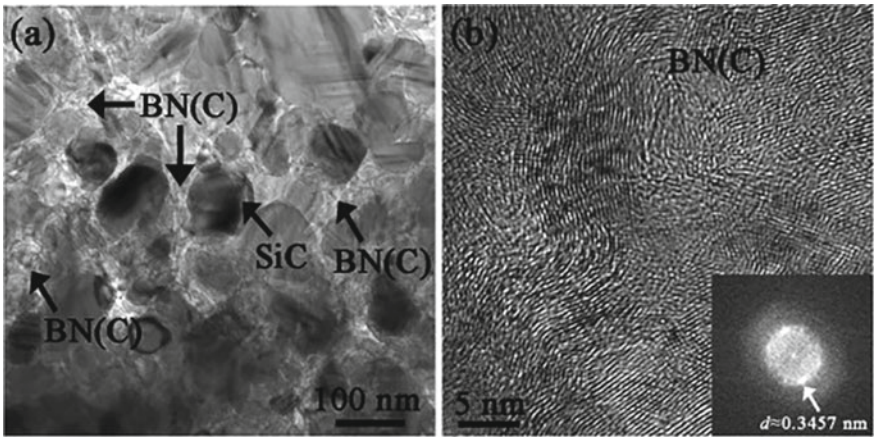

Fig. 1.8 Microstructural feature of MA-Si_2BC_3N monoliths hot-pressed at 1900 °C: **a** Bright filed image showing the shape, size and the distribution of each phase; **b** HRTEM image of turbostratic BN and corresponding fast Fourier transform (FFT) pattern [115]

appear in selected regions. BN(C) grains exhibit a turbostratic structure, as found in PDCs-SiBCN crystalline ceramics. They consist of layers similar to graphite or h-BN, rotated by a random angle around the *c* axis or perpendicular to *c* axis. Therefore, the interplanar spacings along the c axis in turbostratic-BN(C) are generally enlarged by different degrees. The detected (0002) peak of BN(C) shifts towards lower angle by ~0.7° resulting in the expansion of *d*(0002) by 0.009 nm. Coincidently, the fluctuation in interlayer spacings in graphite or h-BN is generally accompanied by rotation, translation or curvature of single layers. The structural distortion and peak shift result in the formation of turbostratic structure with a relatively low three-dimensional order degree. Turbostratic BN(C) is most likely composed of heterogeneously distributed t-carbon layers, t-BN layers and B-doped t-carbon layers.

The formation of turbostratic BN(C) can be attributed to the easy-to-strip character of graphite and h-BN. The fierce collisions during MA break h-BN and graphite into tiny fragments, mix them as uniformly as possible and activate mechanochemical effects leading to formation of B-N-C and B-C-N bonds. Coincidently, h-BN and graphite have similar crystal structure and lattice parameters thus providing chance to the solid solution of carbon in t-BN, or boron and nitrogen in t-carbon. However, the atomic arrangement and chemical bonding states of BN(C) in SiBCN materials developed both by inorganic processing route and by polymer precursor method are still not clearly understood thus requiring further investigations.

The atomic arrangements in SiC and BN(C) phases at and near the interfacial regions are quite different [115]. SiC atoms exhibit long-range order, while BN(C) species have only short- or at best medium-range order. The interfacial regions between the two phases are limited to three or four atomic layers, 0.8–1.1 nm thick.

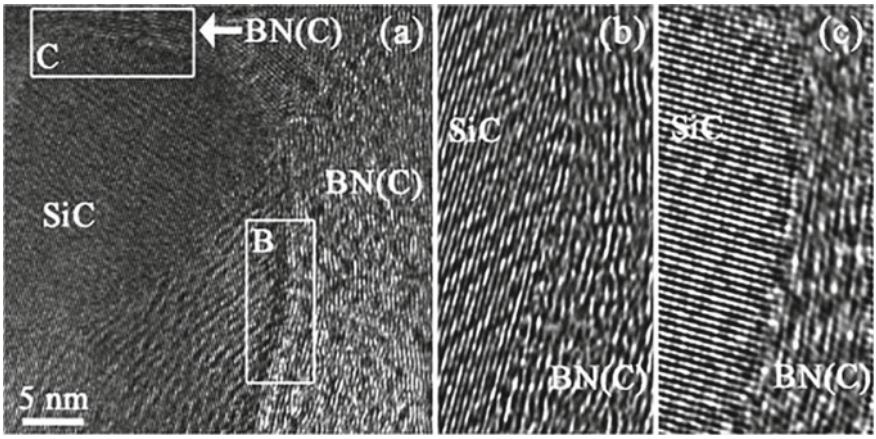

Fig. 1.9 Microstructural features of the interfacial region between SiC and BN(C) in MA- Si_2BC_3N ceramics hot-pressed at 1900 °C: **a** HRTEM image; **b**, **c** inverse FFT images of the areas marked by the white rectangles B and C in (**a**), respectively [115]

No impurity or any other phases like low-melting-point phases form in pure MA-SiBCN monoliths (Fig. 1.9). The "clean" interfacial regions coupled with capsule-like structures hinder long-range atomic diffusion thus limiting the grain growth. This is favorable to the structural stability, resistance to creep and oxidation of the SiBCN materials at high temperatures.

1.3.2 Mechanical Properties

Due to the limits of the sample sizes, only hardness and elastic modulus tests can be performed for the PDCs-SiBCN monoliths, in some cases toughness can also be measured using fracture-mechanics methods, which evaluate the critical value of a crack-driving force [116–122]. Compared to the SiC and Si_3N_4 crystalline ceramics, amorphous PDCs-SiBCN have lower density and Young's modulus, but higher microhardness. The tensile strength of amorphous PDCs-SiBCN ceramic fibers at room temperature is up to 3.2–4.0 GPa and the elastic modulus is in range of 200–210 GPa (Table 1.1). The maximum using temperature of the PDCs-SiBCN fibers in the air can reach to ~ 1500 °C, while their tensile strength at 1500 °C is obtained at ~ 2.3 GPa. The elastic modulus of the PDCs-SiBCN fibers at 1400 °C can still maintain 80–90%. The average thermal expansion coefficient of the PDCs-SiBCN ceramic fibers is 3.5×10^{-6} °C^{-1} [52, 82, 117, 118].

MA-Si_2BC_3N monoliths exhibit excellent mechanical properties including room temperature flexural strength to 400 and 240 MPa at 1400 °C in air, and elastic modulus of 150 GPa. The flexural strength and fracture toughness of MA-Si_2BC_3N are equivalent to pure SiC values. The elastic modulus is 1/3 ~ 1/2 lower than SiC, and

Table 1.1 Comparison of the mechanical properties for the different Si-based ceramic fibers [43]

Properties	SiC	SiOC	SiCTiO	SiN	SiBC	SiBCN	SiBCNO
Room temperature tensile strength (GPa)	3.0–4.0	3.0	2.9	2.1	3.4–4.8	3.2–4.0	4.0
1500 °C tensile strength (GPa)	–	–	–	–	–	1.5	–
Room temperature Young's modulus (GPa)	300–420	190–250	200	220	430	200–210	400
Fracture elongation	0.6–1.0	–	–	–	–	–	–
Thermal expansion coefficient ($\times 10^{-6}$ °C^{-1})	3.3–4.0	–	–	–	–	3.5	–
Density (g/cm^3)	2.74–3.10	2.5	2.5	2.4	3.1	1.8	–
Diameter (μm)	10–14	10–20	8–12	–	8–10	10–12	~ 10

the hardness is ~4/5 lower. The combination of high flexural strength and relatively low elastic modulus contributes to excellent thermal shock resistance [123]. Furthermore, a relative low hardness coupled with the turbostratic structure of BN(C) phase is beneficial to machinability. An increasing ratio of Si: C results in an increasing relative content of α/β-SiC in the as-sintered MA-SiBCN ceramics, leading to a nearly linear increase in mechanical properties. The flexural strength, elastic modulus, fracture toughness and Vickers' hardness of the MA-SiBCN ceramics with a Si: C ratio of 3: 4 are 511 MPa, 157 GPa, 5.64 MPa·$m^{1/2}$ and 5.9 GPa, respectively [124].

The mechanical properties of the as-sintered monoliths are also correlated with the sintering atmosphere [124]. The hot-pressed MA-Si_2BC_3N monoliths sintered in 1 bar N_2 atmosphere show satisfying bulk density, flexural strength, elastic modulus and fracture toughness, higher than those sintered in Ar. For instance, the bending strength of the MA-Si_2BC_3N ceramics sintered in N_2 and Ar, is 526 MPa and 422 MPa, respectively. The Si_2BC_3N-Al monoliths show flexural strength of 527 MPa and fracture toughness of 5.25 MPa $m^{1/2}$. A high N_2 partial pressure inhibits decomposition of some phases during sintering of Si_2BC_3N-Al ceramics. Consequently, the values of density, flexural strength, elastic modulus and fracture toughness of the Si_2BC_3N-Al ceramics sintered in N_2 are much higher than those of sintered counterparts in Ar.

Increases in a boron content results in formation of B_xC and belt-like BN(C) improving the hardness and fracture toughness [4]. Hot-pressed MA-$Si_2B_{1.5}C_2N$ bulk ceramics at 1900 °C provide better mechanical properties: flexural strength of 413 ± 13 MPa, fracture toughness of 5.41 ± 0.91 MPa·$m^{1/2}$, elastic modulus of 213 ± 7 GPa, Vickers' hardness of 7.66 ± 0.32 GPa. Hot-pressed MA-Si_2BC_xN ($2 \leq x \leq 3$) ceramics at the same hot-pressed condition also provide desirable mechanical properties. But an under or over dose of carbon will deteriorate their mechanical properties.

The addition of reasonable Al, Zr, Al–Zr, AlN, ZrO_2, ZrB_2, HfB_2, TaC, ZrC, TaC, Ta_4HfC_5, MgO–ZrO_2–SiO_2 (MZS), MgO–Al_2O_3–SiO_2 (MAS), multi-walled

carbon nanotubes (MWCNTs), or graphene platelets (GPLs), etc. leads to varying improvement on mechanical properties of the MA-Si_2BC_3N materials [43]. Few ZrO_2 addition results in the optimal reinforcing effects, while MZS addition results in the optimal toughening effects. Additionally, a desirable strengthening together with toughening effect is also achieved by adding metal Al particle [125] or MWCNTs. For example, the Si_2BC_3N-Al monoliths show flexural strength of 527 MPa and fracture toughness of 5.25 MPa $m^{1/2}$ (Table 1.2).

The as-sintered MA-SiBCN bulk ceramics exhibit brittle fracture characteristics when loaded at room temperature; however, the C_f/Si_2BC_3N composites display pseudoplastic fracture behavior suggesting potential applications in thermal shock environments [126, 127]. On this basis, the introduction of few ZrO_2 in C_f/Si_2BC_3N composites effectively promotes their densification with moderate interfacial bonding, thereby guaranteeing the fiber pullout and bridging [123]. Nevertheless, the introducing SiC_f cannot improve the fracture toughness of MA-Si_2BC_3N, which still show brittle fracture behavior. However, once h-BN is coated on SiC_f surfaces, the fracture toughness of the SiC_f/SiBCN composites is significantly improved; however, although fiber pullout and crack deflection are observed, and the resulting composites still show catastrophic fracture. Yet if both short C_f and SiC_f are incorporated in MA-Si_2BC_3N matrix, the (C_f-SiC_f)/Si_2BC_3N composites show pseudoplastic fracture characteristics even though lower relative densities and room temperature mechanical properties are obtained. The mechanical properties of the (C_f-SiC_f)/SiBCN composites decrease after introducing Pyrolytic carbon (PyC) or h-BN weak interfaces, but still maintain pseudoplastic fracture characteristics.

1.3.3 Oxidation Resistance and Oxidation Mechanisms

(1) **Oxidation resistance property**

MA derived Si_2BC_3N monoliths both show excellent oxidation resistance in dry air and moist air. Only a thin oxide scale less than 10 μm thick forms on monolithic surfaces oxidized at 1200 °C for 85 h in flowing dry air. The oxide scale thickness is about 200 μm, though the oxidation rate is markedly accelerated in moist air with an absolute humidity of 0.8 g/cm^3. The ternary chemical bonds including C-B-N and B-C-N can effectively lower diffusion of oxygen inward thus leading to improved oxidation resistance superior to SiC-BN monolithic ceramics.

Too much addition of oxygen-sensitive carbon with fine grain sizes, whether free carbon or carbon imbedded into interlayers of h-BN will weaken the oxidation resistance of MA-Si_2BC_xN ($x = 1$–4) monoliths. The excessive introduction of boron into MA-$Si_2B_yC_3N$ ($y = 1.5$–4) is also detrimental to the oxidation property. Too much boron addition causes the rapid consumption of BN(C), B_xC and loss of B_2O_3 thereby promoting the oxidation rate at high temperatures ($\geq$1500 °C).

The Al, Zr, ZrO_2, AlN and MZS etc. additives also have a significant influence on oxidation resistance of MA-$Si_2B_2C_2N$ monolithic ceramics [128–135]. ZrO_2 and AlN

Table 1.2 The bulk density and mechanical properties of the MA-SiBCN monoliths and their ceramic matrix composites prepared by various sintering techniques

Material composition	Density (g/cm^3)	Flexural strength (MPa)	Young's modulus (GPa)	Fracture toughness (MPa·m$^{1/2}$)	Hardness (GPa)	Fracture modes
[a]SiBCN	2.12–2.82	66.3–423.4	30.6–139.4	1.25–3.09	2.4–5.7	Brittle
[b]SiBCN	2.64–2.83	–	220.0–291.0	3.60–4.25	20.0–29.4	Brittle
[c]SiBCN	2.52–2.76	331.0–459.5	120.0–139.4	3.28–4.77	5.7–11.0	Brittle
[d]SiBCN	2.49–2.84	200.0–511.0	133.0–220.0	2.80–5.64	1.5–6.0	Brittle
SiBCN-Zr	3.22–4.08	202.0–400.0	142.1–252.4	2.34–3.16	3.3–9.6	Brittle
SiBCN-Al	2.77–2.90	422.0–527.0	174.0–222.0	3.40–5.25	11.6–12.7	Brittle
SiBCN-(Zr-Al)	2.70–2.75	480.1–590.2	120.4–122.6	4.93–5.60	5.2–5.8	Brittle
SiBCN-Al_4SiC_4	2.65–2.66	345.1–451.5	119.4–128.4	5.17–5.44	6.7–6.9	Brittle
SiBCN-ZrC	2.33–2.64	153.9–229.5	113.4–141.7	1.96–2.25	2.5–3.4	Brittle
SiBCN-TaC	2.61–2.79	351.3–399.5	141.4–164.1	4.04–4.26	5.0–7.2	Brittle
SiBCN-Ta_4HfC_5	2.68–2.79	310.2–344.1	–	3.67–4.52	–	Brittle
[e]SiBCN-ZrB_2	2.82–3.53	315.0–411.0	133.0–172.0	3.50–5.10	3.1–7.8	Brittle
[f]SiBCN-ZrB_2	2.78–2.99	512.3–559.6	163.6–178.9	6.71–6.77	5.2–5.7	Brittle
[g]SiBCN-ZrB_2	3.67–3.74	343.1–386.1	232.8–242.4	4.56–4.84	4.3–4.6	Brittle
SiBCN-HfB_2	3.29–4.91	158.2–176.1	173.5–270.1	3.88–4.17	6.9–7.2	Brittle
SiBCN-(TiB_2-TiC)	2.03–2.80	158.4–311.2	76.1–141.3	1.85–3.92	1.5–7.7	Brittle
SiBCN-ZrO_2	2.83	575.4 ± 73.7	159.2 ± 21.7	3.67 ± 0.01	6.7 ± 0.7	Brittle
SiBCN-AlN	2.74	415.7 ± 147.3	148.4 ± 8.3	4.08 ± 1.18	6.4 ± 1.2	Brittle
SiBCN-MZS	2.78	394.2 ± 41.7	152.9	5.86 ± 0.06	8.3 ± 0.6	Brittle
SiBCN-MAS	2.44–2.58	274.4–425.1	–	–	4.2–6.2	Brittle
SiBCN-$C_{f(PyC)}$	1.92–2.18	30.4–70.5	20.3–55.6	2.24–2.38	0.9–2.3	Pseudoplastic

(continued)

Table 1.2 (continued)

Material composition	Density (g/cm^3)	Flexural strength (MPa)	Young's modulus (GPa)	Fracture toughness (MPa·m$^{1/2}$)	Hardness (GPa)	Fracture modes
SiBCN-(C_f-ZrO_2)	2.39	112.4 ± 12.1	111.1 ± 23.3	2.94 ± 0.25	–	Pseudoplastic
SiBCN-(C_f-MAS)	2.38–2.56	256.9–400.2	–	3.3–4.5	4.2–6.2	Brittle
SiBCN-(C_f-ZrB_2)	2.20–3.36	221.2–405.7	108.8–176.4	3.21–5.25	2.6–4.5	Pseudoplastic
[h]SiBCN-SiC_f	2.35–2.57	70.2–284.3	64.1–183.5	1.04–3.66	–	Brittle
[i]SiBCN-$SiC_{f(BN)}$	2.14–2.20	79.0–101.2	–	1.63–1.94	2.9–4.7	Brittle
[i]SiBCN-($SiC_{f(BN)}$-MAS)	2.69–2.76	318.7–436.6	–	5.87–6.81	9.1–11.4	Brittle
[i]SiBCN-(SiC_f-MAS)	2.69–2.76	363.1–453.3	–	5.50–6.15	10.1–11.2	Brittle
[j]SiBCN-$SiC_{f(BN)}$	2.62–2.70	149.4–208.0	92.9–114.3	2.50–3.92	–	Brittle
[j]SiBCN-(C_f-SiC_f)	2.24	97.2 ± 2.6	83.8 ± 2.5	3.51 ± 0.22	–	Brittle
[j]SiBCN-($C_{f(BN)}$-$SiC_{f(BN)}$)	2.18	69.2 ± 8.5	72.9 ± 8.3	2.60 ± 0.21	–	Pseudoplastic
[j]SiBCN-($C_{f(PyC)}$-$SiC_{f(PyC)}$)	2.04	59.4 ± 5.1	54.0 ± 5.0	2.04 ± 0.31	–	Pseudoplastic
SiBCN-GPLs	2.17–2.45	135.3–196.6	94.6–150.1	3.04–5.40	2.4–5.4	Brittle
SiBCN-MWCNTs	2.58	462 ± 50	115 ± 2	5.54 ± 0.6	5.1 ± 0.2	Brittle
SiBCN-$MWCNTs_{(SiC)}$	2.59–2.61	390.9–532.1	142.5–144.0	5.80–6.66	–	Brittle

[a] Hot-pressed sintering; [b] High-pressure sintering; [c] Hot-isostatic sintering; [d] Spark plasma sintering; [e] Introduction of sol–gel derived ZrB_2; [f] Introduction of MA derived nano ZrB_2; [g] Introduction of Zr and B mixture; [h] Introduction of unmodified SLFC1 SiC_f; [i] Introduction of KD-SA SiC_f; [j] Introduction of KD-II SiC_f

are detrimental to oxidation resistance with oxidation initiated below 1000 °C, and accelerated above 1200 °C. A large number of pores form in the oxide scale ~ 100 μm away from the oxidized surfaces. This could be due to the high diffusion rate of oxygen in ZrO_2 or AlN providing the extra inward diffusion paths for oxygen during composite oxidation. In contrast, MZS significantly improves oxidation resistance. The oxide scale thickness of MZS/$Si_2B_2C_2N$ composite ceramics oxidized at 1500 °C for 10 h is only 10 ~ 20 μm, while it is up to 40 ~ 100 μm for the pure MA-$Si_2B_2C_2N$ oxidized at 1400 °C with a dwell time of several hours.

Significantly, the addition of ultrahigh temperature ceramics (UHTCs) [131, 132], such as ZrB_2, HfB_2, ZrC, Ta_4HfC_5 and TaC, etc. shows higher oxidation resistance beyond 1500 °C due to the formation a three-dimensional oxide skeleton of UHTCs based oxides fulfilled within an amorphous silica glass. For example, the oxide layer thickness of 10 wt.% nano Ta_4HfC_5 containing MA-$Si_2B_2C_2N$ monoliths is only ~ 14.5 μm after oxidation at 1650 °C for 5 h, much lower than ~ 91.9 μm of pure MA-$Si_2B_2C_2N$.

(2) **Oxidation thermodynamics**

As noted above, the as-sintered MA-$Si_2B_2C_2N$ monoliths are composed of α/β-SiC and BN(C) sometimes together with residual amorphous phase. BN(C) consists of heterogeneously distributed t-carbon, t-BN and B-doped t-carbon layers. Therefore, the oxidation of MA-$Si_2B_2C_2N$ likely consists of oxidative attack on the amorphous phases, SiC, h-BN and C.

The oxidation of carbon results in the release of CO and/or CO_2 and coincidently, the oxidation of BN results in the B_2O_3 formation and nitrogen release. The formed liquid-B_2O_3 layer with a melting point of 450 °C uniformly covers the sample surfaces and starts to evaporate at ~ 900 °C. Above 1200 °C, the rapid evaporation of B_2O_3 occurs due to its high vapor pressure [136]. The high temperature oxidation of SiC may be either passive or active depending on the local oxygen concentration. Silica usually forms as a dense protective oxide scale via the passive oxidations at oxygen pressures close to one bar. The reaction can start below 780 °C leading to a net increase in the mass. The SiO_2 scale protects SiC from further catastrophic oxidation to SiO occurring at higher temperatures. Such protective action can theoretically continue up to the melting point of SiO_2 (~ 1720 °C) [137].

However, in cases where the oxidant pressure is less than one bar, the pressure is insufficient to form SiO_2 and SiO form resulting in rapid consumption of SiC via the active oxidations at higher temperatures [138]. At 1200–1300 °C, B_2O_3 can react thermodynamically with SiO_2 forming borosilicate glass [139]. The borosilicate will discompose leading to evaporation of B_2O_3 and even SiO_2 at much higher temperatures. Therefore, the formation of bubbles and loose, porous oxide scale are due primarily to the release of CO, CO_2, N_2 and the evaporation of B_2O_3.

(3) **Oxide scale microstructure**

The oxide scale of MA-$Si_2B_2C_2N$ monoliths show mono- or dual-layer structures depending mainly on the fabrication processing (Fig. 1.10). The hot-pressed MA-$Si_2B_2C_2N$ oxidized at 1300 °C shows a monolayer structural oxide scale, adhered

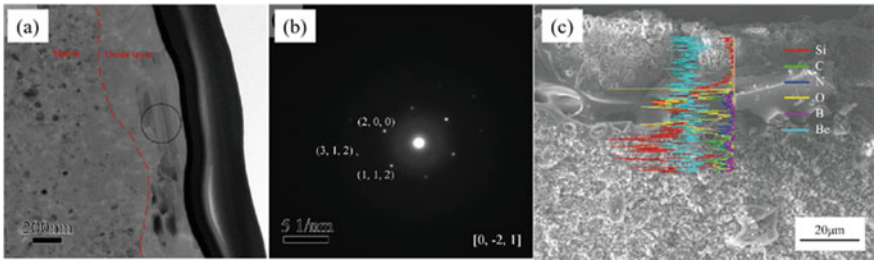

Fig. 1.10 The oxide scale microstructure of the oxidized MA-Si_2BC_3N monoliths consolidated by **a**, **b** HP or **c** SPS: **a**, **b** Oxidized at 1300 °C/1 h in dry flowing air; **c** oxidized at 1200 °C dry air for 85 h [124, 133]

tightly to the ceramic matrix [133]. The oxide scale exhibiting a low degree of crystallinity consists of amorphous SiO_2 and few cristobalite. The MA-$Si_2B_2C_2N$ counterparts prepared by SPS show a dual-layer structural oxide scale [124]. The outer layer is loose and porous which is rich in silicon and oxygen, while the relatively dense inner layer is rich in silicon, oxygen and carbon, together with few boron and nitrogen. The inner layer hinders effectively the inward diffusion of oxygen thus slowing down the oxidation rate.

The oxidation investigation of hot-pressed Zr-containing MA-$Si_2B_2C_2N$ monoliths also indicates a monolayer oxide scale consisting mainly of SiO_2 glass forms on the surfaces at 1500 °C/5 h/air. In contrast, the PDCs-SiBCN materials usually exhibit dual- or multi-layer oxide scale most likely contributing to improved oxidation resistance [82]. It seems reasonable to suggest that thin amorphous oxide scales with a dual-layer structures form on a PDCs-$SiBN_3C$ fiber surfaces in air at high-temperatures responsible for excellent oxidation resistance. The outer layer is composed of silica containing some boron and carbon, while the inner layer is turbostratic B-N phase containing some silicon and oxygen. The PDCs-$SiBN_3C$ fiber shows similar strength to those of polycrystalline SiC fibers, and resistance to oxidation and creep superior to polycrystalline fibers, although the reasons why such microstructure provides better oxidation resistance than single passivating layer of silica are not completely clear.

In another case [140], a tri-layer α-cristobalite/SiO_2/SiBCNO (with BN precipitates) scale forms on a PDCs-$SiBC_{0.8}N_{2.3}$ fiber surfaces heated at 1500 °C for 2 h in air (Fig. 1.11). The unreacted fiber core retains its amorphous nature. The outermost layer oxidized at 1500 °C has devitrified to cristobalite. The second layer consists of essentially pure silica glass. The oxidation layer next to the core consists of amorphous SiBCNO and nanosized turbostratic BN, which evolves into a more oxygen-rich glass with hexagonal and turbostratic BN grains dispersed throughout nearer the surface. This interlayer does not disappear on heating above 1450 °C and is suggested to be the reason for offering 10 times more oxidation resistance than similar coatings of Si_3N_4 and SiC. However, the multilayer oxide scale cannot ensure an expected high-temperature strength which degrades significantly after only short

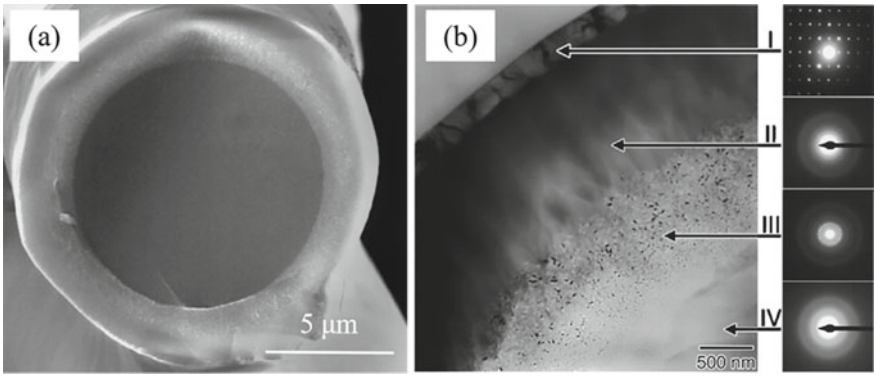

Fig. 1.11 Microstructure of the oxide layer for the amorphous PDCs-$SiBC_{0.8}N_{2.3}$ ceramic fibers after oxidation at 1500 °C for 2 h under dry flowing air condition: **a** SEM cross-section image; **b** bright-field image and corresponding SAED pattern [140]

exposures at temperatures of 1300–1400 °C. Similar oxide scale structure is found for the a PDCs-SiBCN fiber reinforced SiCN composites after air exposure at 1100 °C.

Investigation on a highly dense and amorphous MA-$Si_2B_2C_2N$ monolith prepared by high pressure sintering shows oxidation resistance superior to SiC and Si_3N_4 above 1600 °C, and retains significant resistance to oxidation up to 1800 °C [134]. The microstructure observed for a cross section of the oxidized MA-$Si_2B_2C_2N$ at 1700 °C for 8 h can be divided into three zones from outside to inside: the outermost layer of amorphous N-containing SiO_2; the loose interlayer; the innermost unoxidized amorphous matrix with some nanosized precipitates of SiC and BN(C) (Fig. 1.12). No complex oxide scale like the previously reported two- and tri-layer structures forms here indicating that the good oxidation resistance is not necessarily related to the increasing complexity of oxide scale. No obvious interfaces are observed indicative of strong adhesion between them. Some atomic clusters, which are most likely to be cristobalite, observed in the partial zone close to and beneath the amorphous SiO_2 layer. The loose interlayer mainly includes cristobalite, and unoxidized SiC and BN(C) precipitates.

The formation of dense, passivating surface layers of N-containing amorphous SiO_2 is thus primarily responsible for the excellent oxidation resistance of these amorphous MA-$Si_2B_2C_2N$. Consequently, no necessary correlation exists most likely between the oxidation resistance and the microstructural complicacy of oxide scale, which has been proved by all the investigations up to now.

The phase composition and microstructure of the oxide layers in PDCs-SiBCN ceramic fibers are also impacted by the in-service environment [141]. For example, a PDCs-$SiB_{0.9}C_{1.6}N_{2.4}$ ceramic fiber oxidized at 1400 °C in static air exhibits the three distinct zones with different microstructural feature: (i) Outermost layer of a glass-like structure; (ii) intermediate layer with dispersive nanocrystals; and (iii) innermost homogeneous and amorphous fiber core. All the three zones are dense and intact with no clear boundaries (Fig. 1.13).

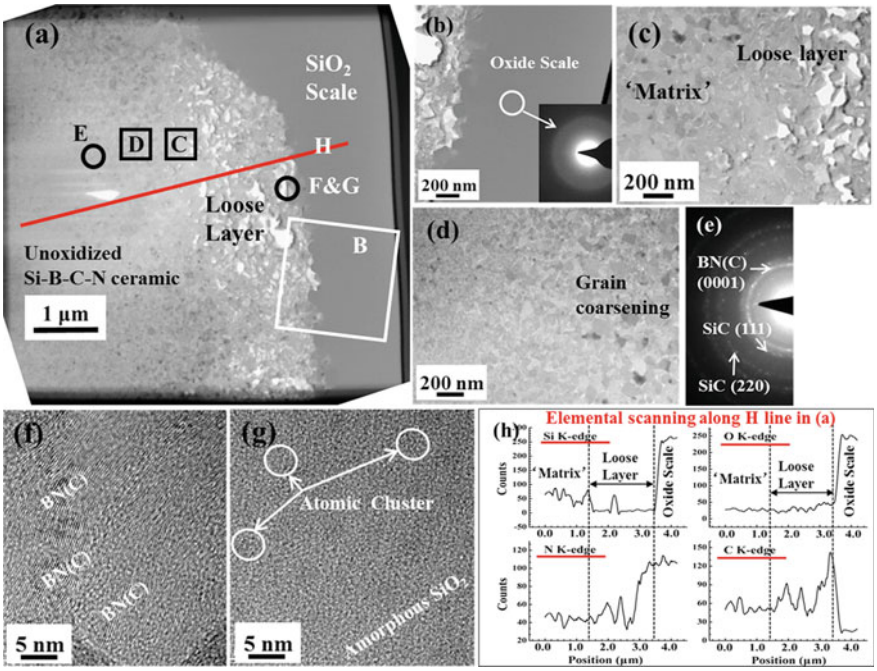

Fig. 1.12 Oxide scale microstructure of a highly dense completely amorphous MA-Si_2BC_3N monolith oxidized at 1700 °C for 8 h: **a** Overview of a cross section; **b–d** magnification of boxes "B, C and D" in (**a**), respectively; **e** SAED pattern of circle "E" in (a); **f**, **g** HRTEM images of circle "F&G" in (**a**); **h** element distribution along the red line "H" in (**a**) [134]

For the PDCs-$SiB_{0.9}C_{1.6}N_{2.4}$ ceramic fiber oxidized at 1400 °C in a simulated combustion environment ($P_{H_2O}/P_{O_2}/P_{N_2}$ = 14:8:78) for 2 h, it also exhibits the three distinct zones: two-layer oxide scale and unoxidized fiber core, which are similar to the former. The outermost layer shows only Si and O elements illustrating the SiO_2. However, its thickness of the outmost layer is ~ 160 nm, which is 300 nm thinner than that of the former (~ 470 nm). Interestingly, the high percentage of water vapor in simulated combustion environment triggers the formation of abundant α-cristobalite nanoparticles dispersing in the outermost amorphous SiO_2 layer, which are absent in fibers corroded in air. The formation of h-BN grains in the interlayer of the two oxide scales can be ascribed to the sacrificial effects of free carbon clusters, Si-C, and Si-N units reacting with oxygen diffusing inward, and thereby improve corrosion resistance of the PDCs-$SiB_{0.9}C_{1.6}N_{2.4}$ fibers under an oxygen- and water-rich atmosphere at high-temperatures.

(4) **Oxidation kinetics**

The oxidation activation energy for amorphous MA-Si_2BC_3N powder (< 0.1 μm) varies from 211.2 (one-step milling) to 561.3 kJ/mol (two-step milling), which are much higher than that of 0.2 μm-sized SiC powder (82.6 kJ/mol) and Si_3N_4 powder (<

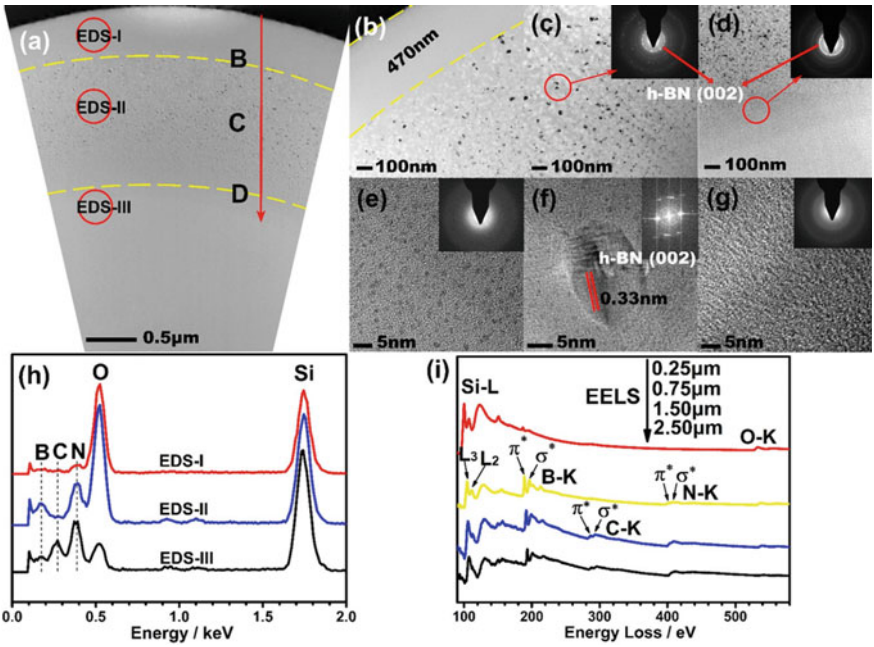

Fig. 1.13 Microstructure of a cross section of the PDCs-$SiB_{0.9}C_{1.6}N_{2.4}$ fiber annealed at 1400 °C in static air for 2 h: **a** Bright-field image; **b**, **d** HRTEM images of the zones marked by "B, C, and D" in (**a**), respectively; **e**, **g** HRTEM images from the glass-like area in (**b**), **c** and amorphous area in **d**; **h** corresponding EDS spectra (I), (II), and (III); **i** EELS spectra with the distance of 0.25, 0.75, 1.50, and 2.50 μm from fiber surface to the inner in (**a**) [141]

100 kJ/mol) [142]. However, the additive of Al results in a poor oxidation resistance. The oxidation activation energy of various Al containing MA-Si_2BC_3N powder (100–200 nm) is 150–220 kJ/mol, much lower than that of pure MA-Si_2BC_3N powder, but still higher than those SiC and Si_3N_4 powders [143]. Besides, the oxidation activation energy decreases with the increasing Al content in MA-Si_2BC_3N powder. In detail, the MA-$Si_2BC_3N_{1.6}Al_{0.6}$ powder (using AlN as Al source) provides oxidation activation energy of 189.0 kJ/mol, higher than that 177.5 kJ/mol of MA-$Si_2BC_3NAl_{0.6}$ (using Al as Al source).

Coincidently, hot-pressed MA-$Si_2BC_3N_{1.6}Al_{0.6}$ monoliths show a low mass change and thin oxide scale compared with $Si_2BC_3NAl_{0.6}$ counterparts under the same oxidation condition (Fig. 1.14). For example, after oxidation at 1400 °C for 80 h, the hot-pressed MA-$Si_2BC_3N_{1.6}A1_{0.6}$ and MA-$Si_2BC_3NAl_{0.6}$ gain weight of ~ 0.58 mg/cm^2 and ~ 0.70 mg/cm^2, respectively. Moreover, the mass change of the two Al-containing materials is higher than that of pure MA-Si_2BC_3N monoliths. That is to say, MA-$Si_2BC_3N_{1.6}Al_{0.6}$ monolithic ceramics show an oxidation resistance superior to $Si_2BC_3NAl_{0.6}$, but inferior to MA-Si_2BC_3N.

Increasing SiC content due to the increasing Si: C ratio in spark plasma sintered monoliths leads to relatively thin and dense oxide scale indicative of superior

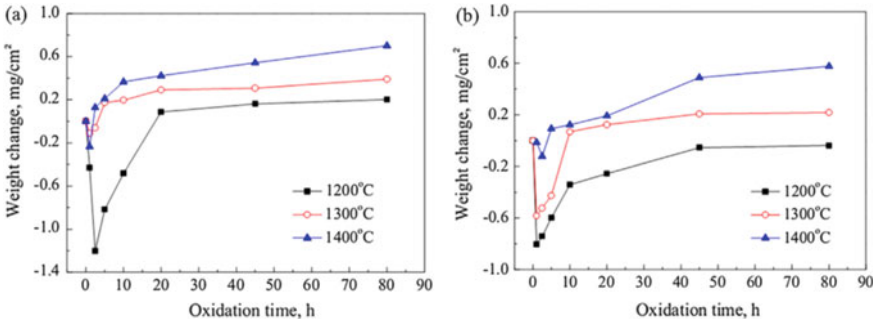

Fig. 1.14 Oxidation kinetic curves of the two hot-pressed Al-containing monoliths oxidized at 1200–1400 °C in flowing air: **a** MA-$Si_2BC_3NAl_{0.6}$ (using Al as the Al source); **b** MA-$Si_2BC_3N_{1.6}Al_{0.6}$ (using AlN as the Al source) [128]

oxidation resistance [43]. Hot-pressed Ta_4HfC_5/Si_2BC_3N composite ceramics have a lower oxidation kinetic constant ~ 215.97 $\mu m^2/h$ at 1600 °C/5 h [144, 145] compared with the MA-Si_2BC_3N counterparts. Nevertheless, the oxide scale growths of GPLs/Si_2BC_3N materials are controlled by a linear kinetic rate law in ranges of 1100–1500 °C indicating a rapid oxidation ratio [146].

The scale growths for the high-pressure sintered amorphous MA-Si_2BC_3N monoliths oxidized at 1500 and 1600 °C fit well to the parabolic laws [135], with kinetics constants of 32.5 $\mu m^2/h$ and 86.1 $\mu m^2/h$, respectively (Fig. 1.15). However, oxidation at 1700 °C becomes complex. The scales grow obeying approximately linear growth for 8 h (with a linear rate constant of 4.0 $\mu m^2/h$), and complying roughly with a parabolic raw within 4 h (with a parabolic rate constant of 79.4 $\mu m^2/h$). They then grow irregularly with oxidation times longer than 8 h. These results suggest the diffusion of oxidant through the growing oxide scales is the rate-controlling process at 1500 and 1600 °C, while the oxidation rate at 1700 °C is co-controlled by the rates of oxidant diffusion through the oxide scale and the reactions on scale/ceramic matrix interfaces. The oxidation activation energy can be deduced to be ~ 116 kJ/mol at 1500–1600 °C below 16 h of oxidation [147]. Note that the values for the apparent activation energies are estimated from the upper and lower extremes of the Arrhenius plot.

For the high-pressure sintered partially crystalline MA-Si_2BC_3N monoliths, their fitted results suggest that at 1500–1600 °C the growth of oxide scales also follows a parabolic law as the oxidation time increases from 0.5 to 16 h, while it is a little bit complicated at 1700 °C [148]. The scale growth follows a linear law within 8 h and also a parabolic trend within 4 h. The faster scale growth for partially crystalline ceramics can be well verified quantitatively by the fitted oxidation rate constant. The aforementioned fitting processing provides parabolic constants of 42.5 $\mu m^2/h$ for 1500 °C/$\leq$ 16 h, 172.2 $\mu m^2/h$ for 1600 °C/$\leq$ 16 h, and 120.4 $\mu m^2/h$ for 1700 °C/$\leq$ 4 h, respectively, for oxidation of partially crystalline MA-Si_2BC_3N bulk ceramic, each of which is larger than those for the completely amorphous counterparts.

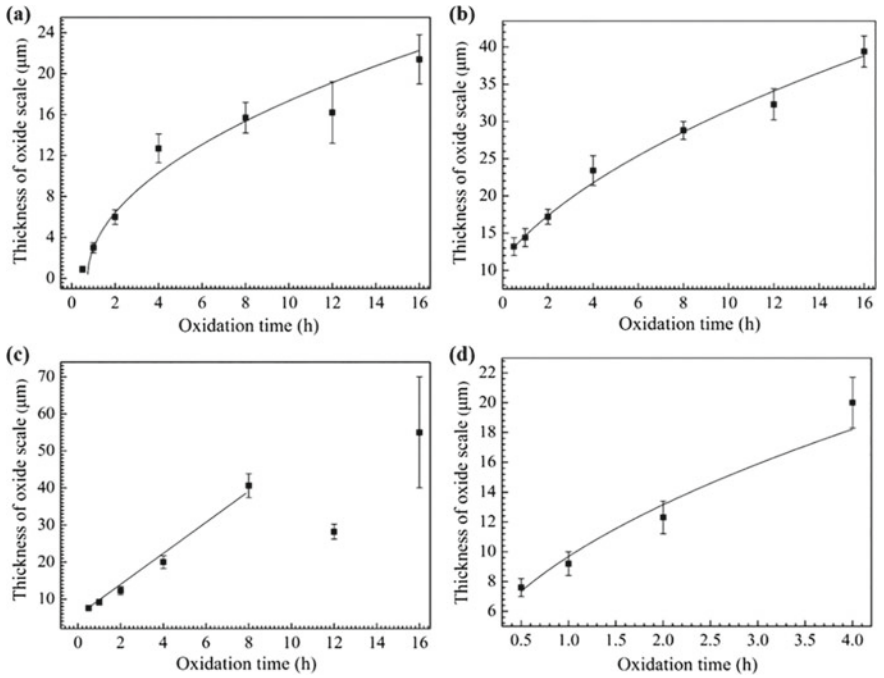

Fig. 1.15 Oxidation kinetic curves of high-pressure sintered amorphous MA-Si_2BC_3N monoliths oxidized in a flowing dry air atmosphere: **a** 1500 °C/≤ 16 h; **b** 1600 °C/≤ 16 h; **c** 1700 °C/≤ 16 h; **d** 1700 °C/≤ 4 h [135]

Oxidation behavior investigation of the amorphous PDC-$Si_{4.46}BC_{7.32}N_{4.40}$ (AMF2p), PDCs-$Si_{2.7}BC_{4.51}N_{2.69}$ (AMF3p) and PDCs-$Si_{3.08}BC_{4.39}N_{2.28}$ (T2/1p) shows that these particles develop thinner scales than pure SiC or Si_3N_4, at least at 1500 °C within 100 h [149]. Scales at 1500 °C in air show a parabolic growth with rate constants of 0.0599 m^2/h (AMF3p) and 0.0593 m^2/h (T2/1p) (Fig. 1.16). The oxidation rate constants are smaller than the determined parabolic rate constants at 1500 °C in oxygen for CVD-SiC (0.095 m^2/h) and CVD-Si_3N_4 (0.113 m^2/h) [150]. Oxidation of the T2/1 particles at 1500 °C for 15 h results in a dense, bubble-free scale. For longer oxidation times of 24 h and even up to 100 h, bubbles form almost completely limited to the so-called "edges" of the thermolyzed particles indicating good oxidation resistance.

Note that the kinetic data of the amorphous AMF2p particles do not obey a parabolic equation. In particular, their oxide scale thicknesses during the short-time experiments are noticeably above the parabolic fit. Nickel et al. have measured their mass changes occurring during the oxidation; however, the obtained results are not easily interpreted. In another work, Müller et al. [151] have reported the parabolic rates for amorphous PDCs-$SiC_{1.6}N_{1.1}B_{0.37}Al_{0.13}$, higher than those of PDCs-SiBCN materials.